Directional Wavelet Packets for Image Processing

Amir Averbuch and Valery Zheludev

Abstract The paper presents a versatile library of quasi-analytic complex-valued wavelet packets originated from polynomial splines of arbitrary orders. The real parts of quasi-analytic wavelet packets are regular spline-based orthonormal wavelet packets derived from discretized periodic polynomial splines. Imaginary parts are the so-called complementary orthonormal wavelet packets derived from the Hilbert transforms of regular wavelet packets. The discrete Fourier transforms of quasi-analytic wavelet packets are located in either the positive or negative half-band of the frequency domain. Consequently, the discrete Fourier transforms of 2D wavelet packets, which are derived by as the tensor products of 1D wavelet packets, occupy one of the quadrants of the 2D frequency domain. Such a structure results in the directionality of their real parts. The shapes of real quasi-analytic wavelet packets are close to windowed cosine waves that oscillate in several different directions at different frequencies. The paper provides a few examples of the successful application of designed quasi-analytic wavelet packets to image denoising and inpainting.

1 Introduction

It is apparent that for an image processing algorithm to be efficient, it has to take into considerations features that characterize the images, such as edges oriented in various directions, texture patterns, that can be approximated by patches oscillating in various directions with various frequencies, and smooth regions. The ability to extract such features even from degraded images is a key element for image denoising, inpainting, deblurring, classification and target detection. This stems from the fact that practically all the processed images have a sparse representation in a proper transform domain. The sparse representation of an image means that it can be

Amir Averbuch · Valery Zheludev (✉)
School of Computer Science, Tel Aviv University, Tel Aviv 69978, Israel, e-mail: zhel@tauex.tau.ac.il

approximated by a linear combination of a relatively small number of 2D "basic" elements selected from a versatile collection called dictionary, while retaining the above mentioned components of the image.

Such a dictionary should comprise a variety of waveforms which are able to capture edges oriented in any direction, texture patches oscillating with any frequency and to represent smooth regions by a very few elements. The latter requirement can be fulfilled if the dictionary elements possess vanishing moments at least locally. In order to meet the former two, the dictionary elements have to be oriented in multiple directions and to have oscillating structures with multiple frequencies.

Image processing applications are characterized by extensive research, especially in recent decades. Naturally, a number of dictionaries are reported in the literature and applied to image processing. We mention contourlets [13], curvelets [9, 8], pseudo-polar Fourier transforms [1, 2] and shearlets [22, 23]. These dictionaries are used in various image processing applications. However, while these dictionaries successfully capture edges in images, they did not demonstrate a satisfactory texture restoration due to lack of oscillating waveforms in the dictionaries.

A number of publications [18, 7, 16, 15, 17, 19, 20], to name a few, design directional dictionaries by tensor multiplication of complex wavelets [21, 24], wavelet frames and wavelet packets (WPs). The tight tensor-product complex wavelet frames (TP_$\mathbb{C}$TF$_n$)[1] with a different number of directions, are designed in [16, 17, 15] and some of them, in particular cptTP_$\mathbb{C}$TF$_6$, TP_$\mathbb{C}$TF$_6$ and TP_$\mathbb{C}$TF$_6^{\downarrow}$, demonstrate impressive performance for image denoising and inpainting. The waveforms in these frames are oriented in 14 directions and, due to the 2-layer structure of their spectra, they possess certain, although limited, oscillatory properties. The *Digital Affine Shear Filter Transform with 2-Layer Structure (DAS-2)* algorithm [10], the two-layer structure inherent in the TP_$\mathbb{C}$TF$_6$ frames, is incorporated into shearlet-based directional filter banks introduced in [28]. This improves the performance of DAS-2 in comparison to TP_$\mathbb{C}$TF$_6$ for texture-rich images such as "Barbara", which is not the case for smoother images like "Lena".

We succeeded in the design of a family of dictionaries that maximally meet the requirements for image processing applications. As a base for such a design, we have a library of orthonormal WPs originating from the discretized polynomial splines of multiple orders (see [3]). The waveforms in the library are symmetric, well localized in time domain, their shapes vary from low-frequency smooth curves to high-frequency oscillating transients. They can have any number of local vanishing moments. Their spectra provide a variety of refined splits of the frequency domain and the shapes of the magnitude spectra tend to a rectangular as the spline's order increases. Their tensor products possess similar properties that are extended to 2D setting while the directionality, which is of crucial importance for image processing, does not exist. However, the directionality is achieved by the extension of these orthonormal WPs to the complex-valued quasi-analytic WPs (qWPs) (see Sect. 2).

[1] The index n refers to the number of filters in the underlying one-dimensional complex tight framelet filter bank.

The paper is organized as follows. Section 2 outlines the design of directional qWPs originated from polynomial splines and the corresponding transforms. Section 3 presents a couple of examples of image denoising and inpainting. Section 4 comprises a brief discussion.

The following abbreviations are used:

1D	One-dimensional
2D	Two-dimensional
cWP	Complementary wavelet packet
DFT	Discrete Fourier transform
dWP	Orthonormal discretized polynomial spline of different orders
FFT	Fast Fourier transform
HT	Hilbert transform
qWP	Quasi-analytic wavelet packet
PSNR	Peak Signal to Noise Ratio
SSIM	Structural Similarity Index [27]

2 Quasi-analytic Directional Wavelet Packets

In this section, we depict the properties of qWPs and give some illustrations. An outline of the qWPs design and the implementation of the corresponding transforms is provided in [6], which describes the successful application of qWPs to image inpainting. A detailed description of the design and implementation is given in [4].

2.1 Properties of qWPs

The qWPs are derived from the periodic WPs originating from orthonormal discretized polynomial splines of different orders (dWPs), which are described in [3, Chap. 4] (a brief outline is given in [4]). The dWPs are denoted by $\psi^p_{[m],l}$, where p is the generating spline's order, m is the decomposition level and $l = 0, \ldots 2^m - 1$, is the index of a m-level wavelet packet. The 2^m-sample shifts

$$\{\psi^p_{[m],l}(\cdot - 2^m k)\}, \quad l = 0, \ldots, 2^m - 1,\ k = 0, \ldots, N/2^m - 1,$$

of the m-level dWPs form an orthonormal basis of the space $\Pi[N]$ of N-periodic discrete-time signals. Surely, other orthonormal bases are possible, for example, the wavelet and Best bases [11].

The spaces of 1D and 2D N-periodic signals are denoted by $\Pi[N]$ and $\Pi[N, N]$, respectively. We denote $N = 2^j$ and $\omega \stackrel{\text{def}}{=} e^{2\pi\, i/N}$. The sequence $\delta[k] \in \Pi[N]$ is the N-periodic Kronecker delta. Discrete Fourier Transform (DFT) of a signal $\mathbf{x} \in \Pi[N]$ is the N-periodic complex sequence

$$\hat{x}[n] = \sum_{k=0}^{N-1} \omega^{-kn} x[k], \quad n \in \mathbb{Z}.$$

Complementary wavelet packets (cWPs) are $\phi^p_{[m],l}$ and $\phi^p_{[m],j,l}$ and quasi-analytic wavelet packets (qWPs) $\Psi^p_{\pm[m],l}$ and $\Psi^p_{+\pm[m],l,j}$ in 1D and 2D cases, respectively.

2.1.1 One-dimensional qWPs

The waveforms $\psi^p_{[m],l}[k]$ are symmetric, well localized in the spatial domain and have oscillatory structure, their DFT spectra form a refined split of the frequency domain. The shapes of the magnitude spectra tend to rectangular as the spline's order p grows. A common way to extend 1D WP transforms to multiple dimensions is by the tensor-product extension. The 2D dWPs from the level m are:

$$\psi^p_{[m],j,l}[k,n] \stackrel{\text{def}}{=} \psi^p_{[m],j}[k]\,\psi^p_{[m],l}[n].$$

Their 2^m-sample shifts along vertical and horizontal directions form orthonormal bases of the space $\Pi[N,N]$ of 2D signals $N-$periodic in both directions. The drawback is the lack of directionality. The directionality is achieved by switching to complex wavelet packets.

For this, we start with the application of the Hilbert transform (HT) to the dWPs $\psi^p_{[m],l}$, to get the signals

$$\tau^p_{[m],l} = H(\psi^p_{[m],l}), \quad m = 1,...,M,\ l = 0,...,2^m-1.$$

A slight correction of these signals

$$\phi^p_{[m],l}[k] \stackrel{\text{def}}{=} \hat{\psi}^p_{[m],l}[0]/N + \hat{\psi}^p_{[m],l}[N/2]/N + \tau^p_{[m],l}[k] \tag{1}$$

provides us with a set of signals from the space $\Pi[N]$, whose properties are similar to the properties of the dWPs $\psi^p_{[m],l}$. In particular, their shifts form orthonormal bases in $\Pi[N]$, their magnitude spectra coincide with the magnitude spectra of the dWPs $\psi^p_{[m],l}$. However, unlike the symmetric dWPs $\psi^p_{[m],l}$, the signals $\phi^p_{[m],l}$ are antisymmetric for all l except for $l_0 = 0$ and $l_m = 2^m - 1$. We refer to the signals $\phi^p_{[m],l}$ as the complementary orthonormal WPs (cWPs).

The sets of complex-valued WPs, which we refer to as the quasi-analytic wavelet packets (qWPs), are defined as

$$\Psi^p_{\pm[m],l} = \psi^p_{[m],l} \pm i\phi^p_{[m],l}, \quad m = 1,...,M,\ l = 0,...,2^m-1,$$

where $\phi^p_{[m],l}$ are the cWPs defined in (1). The qWPs $\Psi^p_{\pm[m],l}$ differ from the analytic WPs by adding two values $\pm i\,\hat{\psi}^p_{[m],l}[0]$ and $\pm i\,\hat{\psi}^p_{[m],l}[N/2]$ into their DFT spectra,

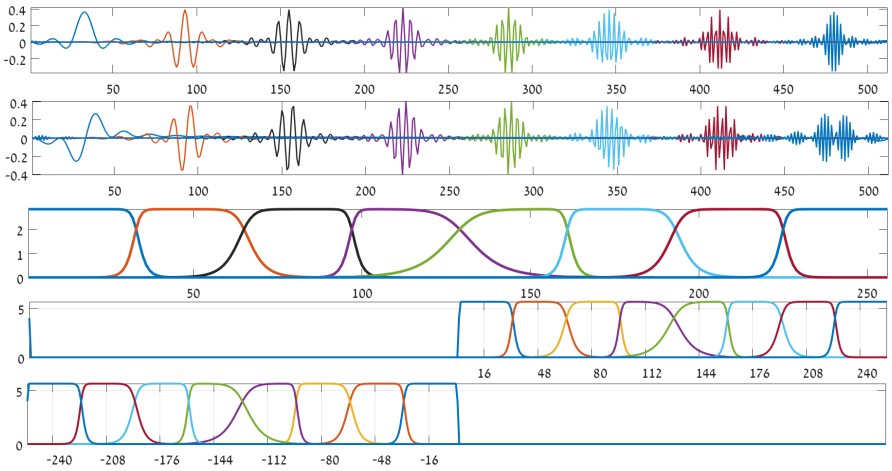

Fig. 1 Top to bottom: signals $\psi^9_{[3],l}$; signals $\phi^9_{[3],l}$, $l = 0, \ldots, 7$; their magnitude DFT spectra (right half-band); magnitude DFT spectra of complex qWPs $\Psi^9_{+[3],l}$; same for $\Psi^9_{-[3],l}$, $l = 0, \ldots, 7$

respectively. The DFT spectra of the qWPs $\Psi^p_{+[m],l}$ are located within positive half-band of the frequency domain and vice versa for the qWPs $\Psi^p_{-[m],l}$.

Figure 1 displays the signals $\psi^9_{[3],l}$ and $\phi^9_{[3],l}$, $l = 0, \ldots, 7$, from the third decomposition level and their magnitude spectra (right half-band), that coincide with each other. Adding $\hat{\psi}^9_{[3],l}[0]$ and $\hat{\psi}^9_{[3],l}[N/2]$ to the spectra of $\phi^9_{[3],l}$, $l = 0, 7$, results in an antisymmetry distortion. These WPs provide a collection of diverse symmetric and antisymmetric well localized waveforms, which range from smooth wavelets for $l = 0, 1$ to fast oscillating transients for $l = 5, 6, 7$. Thus, this collection is well suited to catch smooth as well as oscillating local patterns in signals. In the 2D case, these valuable properties of the spline-based wavelet packets are completed by the directionality of the tensor-product waveforms.

2.1.2 Two-dimensional qWPs

Similarly to the 2D dWPs $\psi^p_{[m],j,l}[k, n]$, the 2D cWPs $\phi^p_{[m],j,l}[k, n]$ are defined as the tensor products of 1D WPs such that

$$\phi^p_{[m],j,l}[k, n] = \phi^p_{[m],j}[k]\, \phi^p_{[m],l}[n].$$

The 2^m-sample shifts of the cWPs $\{\phi^p_{[m],j,l}\}$, $j, l = 0, \ldots, 2^m - 1$, in both directions form an orthonormal basis for the space $\Pi[N, N]$ of arrays that are N-periodic in both directions.

The 2D dWPs $\{\psi^p_{[m],j,l}\}$ as well as the cWPs $\{\phi^p_{[m],j,l}\}$ lack the directionality property which is needed in many applications that process 2D data. However,

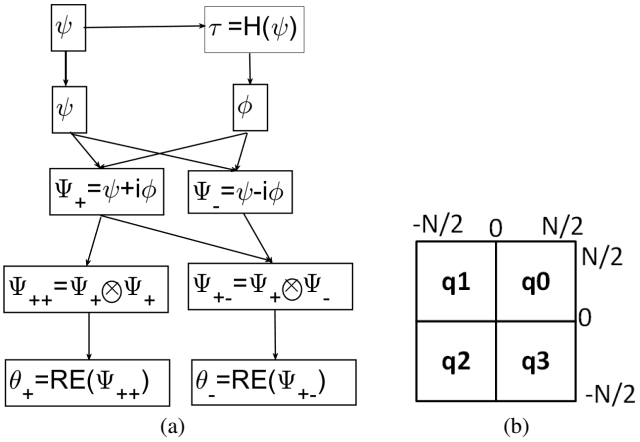

Fig. 2 **a** Diagram of the qWP design; **b** Quadrants of frequency domain

real-valued 2D wavelet packets oriented in multiple directions can be derived from tensor products of complex quasi-analytic qWPs $\Psi^p_{\pm[m],\rho}$. The complex 2D qWPs are defined as follows:

$$\Psi^p_{++[m],j,l}[k,n] \stackrel{\text{def}}{=} \Psi^p_{+[m],j}[k]\,\Psi^p_{+[m],l}[n],$$
$$\Psi^p_{+-[m],j,l}[k,n] \stackrel{\text{def}}{=} \Psi^p_{+[m],j}[k]\,\Psi^p_{-[m],l}[n],$$

where $m = 1,...,M$, $j,l = 0,...,2^m-1$, and $k,n = 0,...,N-1$. The real parts of these 2D qWPs are

$$\begin{aligned}\theta^p_{+[m],j,l}[k,n] &\stackrel{\text{def}}{=} \Re\mathfrak{e}(\Psi^p_{++[m],j,l}[k,n]) = \psi^p_{[m],j,l}[k,n] - \phi^p_{[m],j,l}[k,n],\\ \theta^p_{-[m],j,l}[k,n] &\stackrel{\text{def}}{=} \Re\mathfrak{e}(\Psi^p_{+-[m],j,l}[k,n]) = \psi^p_{[m],j,l}[k,n] + \phi^p_{[m],j,l}[k,n],\end{aligned} \tag{2}$$

Figure 2(a) illustrates the design of qWPs.

The DFT spectra of the 2D qWPs $\Psi^p_{++[m],j,l}$, $j,l = 0,...,2^m-1$, are tensor products of the one-sided spectra of the qWPs

$$\hat{\Psi}^p_{++[m],j,l}[p,q] = \hat{\Psi}^p_{+[m],j}[p]\,\hat{\Psi}^p_{+[m],l}[q]$$

and, as such, they fill the quadrant $\mathbf{q}_0$ of the frequency domain, while the spectra of $\Psi^p_{+-[m],j,l}$, $j,l = 0,...,2^m-1$, fill the quadrant $\mathbf{q}_1$ (see Fig. 2). Figure 3 displays the magnitude spectra of the ninth-order 2D qWPs $\Psi^9_{++[2],j,l}$ and $\Psi^9_{+-[2],j,l}$ from the second decomposition level.

Figure 3 shows that the DFT spectra of the qWPs $\Psi^9_{+\pm[m],j,l}$ effectively occupy relatively small squares in the frequency domain. For deeper decomposition levels, sizes of the corresponding squares decrease as geometric progression. Such config-

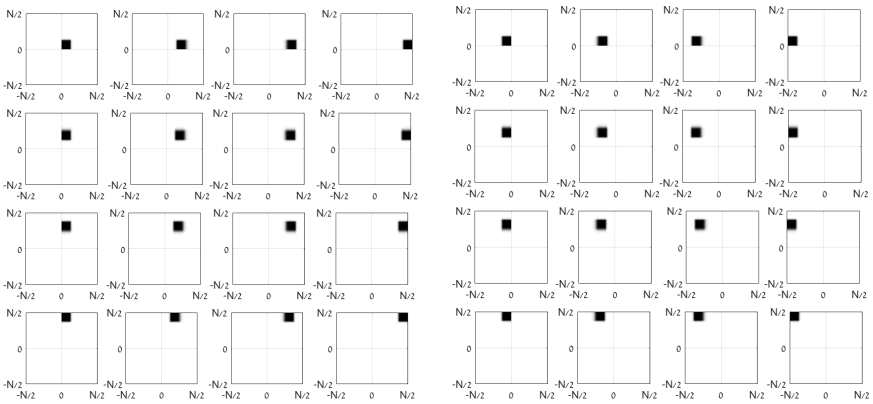

(a) $\Psi^9_{++[2],j,l}$ (b) $\Psi^9_{+-[2],j,l}$

Fig. 3 Magnitude spectra of 2D qWPs from the second decomposition level

uration of the spectra leads to the directionality of the real-valued 2D WPs $\theta^p_{\pm[m],j,l}$ defined in (2). The directionality of the WPs $\theta^p_{\pm[m],j,l}$ is discussed in [4]. It is established that if the spectrum of WP $\Psi^p_{+\pm[m],j,l}$ occupies a square whose center lies in the point $[\kappa_0, \nu_0]$, then the respective real-valued WP $\theta^p_{\pm[m],j,l}$ is represented by

$$\theta^p_{\pm[m],j,l}[k,n] \approx \cos\frac{2\pi(\kappa_0 k + \nu_0 n)}{N}\,\theta[k,n],$$

where $\theta[k,n]$ is a spatially localized low-frequency waveform which does not have a directionality.

But the 2D signal $\cos\frac{2\pi(\kappa_0 k+\nu_0 n)}{N}$ oscillates in the direction $\mathbf{D}$, which is orthogonal to the vector $\mathbf{V} = \kappa_0\mathbf{i} + \nu_0\mathbf{j}$. Therefore, WP $\theta^p_{\pm[m],j,l}$ can be regarded as the directional cosine wave modulated by a localized low-frequency signal θ. The cosine frequencies in the vertical and horizontal directions are determined by the indices j and l, respectively, of the WP $\theta^p_{\pm[m],j,l}$. The bigger the index is, the higher is the frequency in the respective direction. The situation is illustrated in Fig. 4. The imaginary parts of the qWPs $\Psi^p_{+\pm[m],j,l}$ have a similar structure. Figures 5 and 6 display the WPs $\theta^9_{+[2],j,l}$, and $\theta^9_{-[2],j,l}$, $j,l = 0,1,2,3$, from the second decomposition level and their magnitude spectra, respectively. WPs $\theta^9_{+[3],j,l}$ and $\theta^9_{-[3],j,l}$, $j,l = 0,1,...,7$, from the third decomposition level are shown in Fig. 7.

Remark 1 Note that all the WPs $\theta^p_{+[m],j,l}$ whose spectra are located along the vector $\mathbf{V}$, have approximately the same orientation. It is shown in Figs. 5, 6 and 7. For example, all the "diagonal" qWPs $\{\theta^p_{\pm[m],j,j}\}$, $j = 0,...,2^m - 1$, are oscillating with different frequencies in the directions of either 135° (for θ_+) or 45° (for θ_-). Consequently, the number of orientations of the m-th level WPs is less than 2×4^m which is the number of WPs. These orientational numbers are given in Table 1.

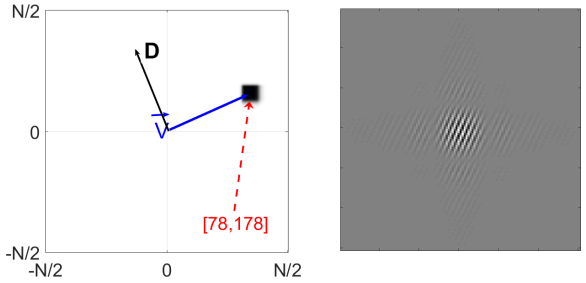

Fig. 4 **a** Magnitude spectra of 2D qWP $\Psi^{p}_{++[3],2,5}[k,n]$; **b** WP $\theta^{p}_{++[3],2,5} = \Re\mathfrak{e}(\Psi^{p}_{++[3],2,5})$

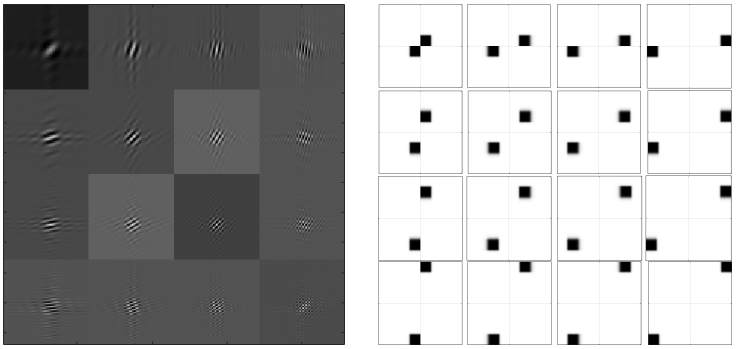

Fig. 5 **a** WPs $\theta^{9}_{+[2],j,l}$ from the second decomposition level; **b** Their magnitude spectra

Table 1 Numbers of different orientations of qWPs $\{\theta^{p}_{\pm[m],j,l}\}$, $j,l = 0,\ldots,2^m-1$, for different decomposition levels

Level m	Number of directions
1	6
2	22
3	86
4	314
5	1218
6	4606

2.2 Implementation Scheme for 2D qWP Transforms

The spectra of 2D qWPs $\{\Psi^{p}_{++[m],j,l}\}$, $j,l = 0,\ldots,2^m-1$, fill the quadrant $\mathbf{q}_0$ of the frequency domain (see Fig. 2), while the spectra of 2D qWPs $\{\Psi^{p}_{+-[m],j,l}\}$ fill the quadrant $\mathbf{q}_1$. Consequently, the spectra of the real-valued 2D WPs $\{\theta^{p}_{+[m],j,l}\}$,

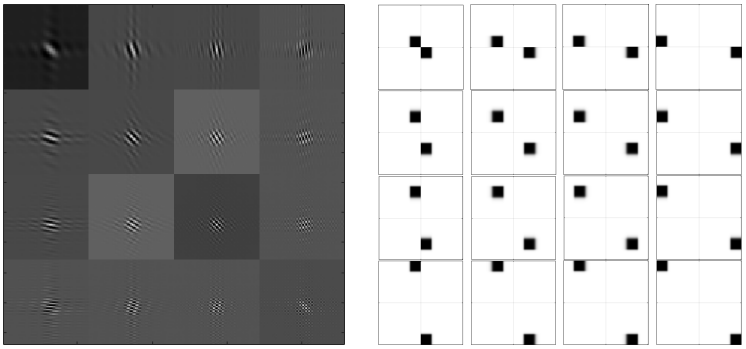

(a) (b)

Fig. 6 **a** WPs $\theta^9_{-[2],j,l}$ from the second decomposition level; **b** Their magnitude spectra

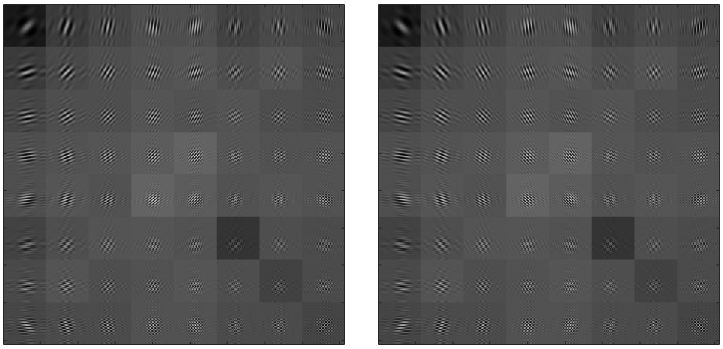

(a) $\theta^9_{+[3],j,l}$ (b) $\theta^9_{-[3],j,l}$

Fig. 7 WPs from the third decomposition level

$j,l = 0,...,2^m - 1$, and $\{\theta^p_{-[m],j,l}\}$ fill the pairs of quadrant $\mathbf{q}_+ = \mathbf{q}_0 \cup \mathbf{q}_2$ and $\mathbf{q}_- = \mathbf{q}_1 \cup \mathbf{q}_3$, respectively. By this reason, none linear combination of the WPs $\{\theta^p_{+[m],j,l}\}$ and their shifts can serve as a basis in the signal space $\Pi[N,N]$. The same is true for WPs $\{\theta^p_{-[m],j,l}\}$. However, combinations of the WPs $\{\theta^p_{\pm[m],j,l}\}$ provide frames of the space $\Pi[N,N]$.

The transforms are implemented in the frequency domain using modulation matrices of the filter banks, which are built from the corresponding wavelet packets. It is important to mention that the structure of the filter banks $\mathbf{Q}_+$ and $\mathbf{Q}_-$ for the first decomposition level is different for the transforms with the "positive" $\Psi^p_{+[m],l}$ and "negative" $\Psi^p_{-[m],l}$ qWPs, respectively. However, the transforms from the first to the second and further decomposition levels are executed using the same filter banks $\mathbf{H}_m$ for the "positive" and "negative" qWPs. This fact makes it possible a parallel implementation of the transforms.

The one-level 2D qWP transforms of a signal $\mathbf{X} = \{X[k,n]\} \in \Pi[N,N]$ are implemented by a tensor-product scheme. To be specific, for the transform with $\Psi^p_{++[1]}$,F the 1D transform of columns from the signal $\mathbf{X}$ is executed using the filter bank $\mathbf{Q}_+$, which is followed by the 1D transform of rows of the produced coefficient arrays using the same filter bank $\mathbf{Q}_+$. These operations produce the transform coefficient array

$$\mathbf{Z}_{+[1]} = \bigcup_{j,l=0}^{1} \mathbf{Z}^{j,l}_{+[1]}$$

comprising of four blocks. The transform with $\Psi^p_{+-[1]}$ is implemented by a subsequent application of the filter banks $\mathbf{Q}_+$ and $\mathbf{Q}_-$ to columns from the signal $\mathbf{X}$ and rows of the produced coefficient arrays, respectively. This results in the coefficient array

$$\mathbf{Z}_{-[1]} = \bigcup_{j,l=0}^{1} \mathbf{Z}^{j,l}_{-[1]}.$$

The further transforms starting from the arrays $\mathbf{Z}_{+[1]}$ and $\mathbf{Z}_{-[1]}$ produce two sets of the coefficients

$$\left\{\mathbf{Z}_{+[m]} = \bigcup_{j,l=0}^{2^m-1} \mathbf{Z}^{j,l}_{+[m]}\right\}, \quad \left\{\mathbf{Z}_{-[m]} = \bigcup_{j,l=0}^{2^m-1} \mathbf{Z}^{j,l}_{-[m]}\right\}, \quad m = 2,...,M,$$

respectively. The transforms are implemented by the application of the same filter banks $\mathbf{H}_m$, $m = 2,...,M$, to rows and columns of the "positive" and "negative" coefficient arrays. The coefficients from a level m comprise of 4^m "positive" blocks of coefficients $\{\mathbf{Z}^{j,l}_{+[m]}\}$, $l,j = 0,...,?^{2^m-1}$, and the same number of "negative" blocks $\{\mathbf{Z}^{j,l}_{-[m]}\}$.

The coefficients from a block are inner products of the signal $\mathbf{X} = \{X[k,n]\} \in \Pi[N,N]$ with the shifts of the corresponding wavelet packet:

$$Z^{j,l}_{\pm[m]}[k,n] = \sum_{\lambda,\mu=0}^{N-1} X[\lambda,\mu]\, \Psi^p_{+\pm[m],j,l}[\lambda - 2^m k, \mu - 2^m n],$$

$$Y^{j,l}_{\pm[m]}[k,n] = \Re\mathfrak{e}(Z^{j,l}_{\pm[m]}[k,n]) = \sum_{\lambda,\mu=0}^{N-1} X[\lambda,\mu]\, \theta^p_{\pm[m],j,l}[\lambda - 2^m k, \mu - 2^m n].$$

The inverse transforms are implemented accordingly. Prior to the reconstruction, some, possibly different, structures (e.g., 2D wavelet, Best Basis or single-level wavelet packets) in the sets $\{\mathbf{Z}^{j,l}_{+[m]}\}$ and $\{\mathbf{Z}^{j,l}_{-[m]}\}$, $m = 1,...M$, are defined, and some manipulations of the coefficients (e.g., thresholding, shrinkage, l_1 minimization) are executed.

The reconstruction produces two complex arrays $\mathbf{X}_+$ and $\mathbf{X}_-$. The signal $\mathbf{X}$ is restored by $\tilde{\mathbf{X}} = \Re\mathfrak{e}(\mathbf{X}_+ + \mathbf{X}_-)/8$. Figure 8 illustrates the "Fingerprint" image restora-

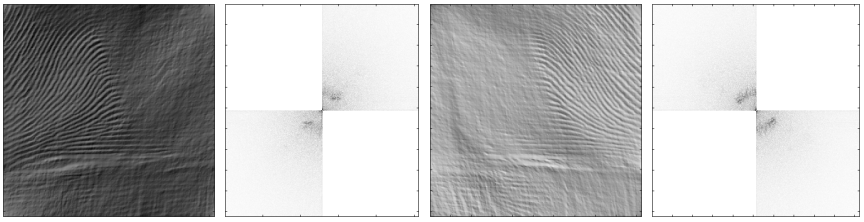

(a) (b) (c) (d)

Fig. 8 **a** Image $\mathfrak{Re}(\mathbf{X}_+)$; **b** Its magnitude DFT spectrum; **c** Image $\mathfrak{Re}(\mathbf{X}_-)$; **d** Its magnitude DFT spectrum

tion by the 2D signals $\mathfrak{Re}(\mathbf{X}_\pm)$. The signal $\mathfrak{Re}(\mathbf{X}_-)$ captures oscillations oriented to *north-east*, while $\mathfrak{Re}(\mathbf{X}_+)$ captures oscillations oriented to *north-west*. The signal $\tilde{\mathbf{X}} = \mathfrak{Re}(\mathbf{X}_+ + \mathbf{X}_-)/8$ perfectly restores the image achieving PSNR = 312.3538 dB.

2.3 Summary of 2D qWPs

The qWP waveforms have the following characteristics:

1. The qWP waveforms are oriented in multiple directions;
2. The qWP waveforms have oscillating structure with multiple frequencies;
3. The qWP waveforms have local vanishing moments;
4. The qWP waveforms are well localized in the spatial domain;
5. The DFT spectra of the qWPs produce a refined frequency separation;
6. The corresponding transforms are implemented in a fast way using the FFT;
7. The transform coefficients have a clear (explainable) physical meaning.

Due to a variety of orientations, the qWPs capture edges even in severely degraded images and their oscillatory shapes with a variety of frequencies enable to recover fine structures. Multiple experiments on image denoising [5] and inpainting [6] demonstrate that qWP-based methods are quite competitive with the best state-of-the-art algorithms.

However, qWPs have a strong potential to handle a new important class of problems. Namely, the above properties of qWPs provide a perfect tool for feature extraction from images and, in that capacity, can serve as a significant component for Deep Neural Networks (DNNs). Due to the versatility of testing waveform and, most importantly, the explanatory physical meaning of the transform coefficients resulting from image convolution with a variety of qWPs waveforms, it is possible to replace at least some of the convolution layers in convolutional DNNs by convolving the image with qWPs. This will lead to a significant reduction of the training dataset size. Our preliminary experiments demonstrate the feasibility of qWPs for such a task.

3 Numerical Examples

In this section, we present several examples.

3.1 Image Denoising

The BM3D algorithm [12] is one of the best image denoising method that exploits the self-similarity of patches and sparsity of the image in a transform domain. This method is efficient in restoration of moderately noised images. However, the BM3D tends to over-smooth and to smear the image fine structure and edges when noise is strong. Also, the BM3D is unsuccessful when the image contains many edges oriented in multiple directions. On the other hand, algorithms that use directional oscillating waveforms provide the opportunity to capture lines, edges and texture details. Therefore, it is natural to combine the qWP-based and BM3D algorithms in order to retain strong features of both algorithms and to get rid of their drawbacks. The description of two hybrid qWP BM3D algorithms and results of multiple experiments on image denoising are presented in a paper submitted to a journal (see the preprint [5]).

The original four images of the experiments are "Fingerprint", "Fabric", "Bridge" and "Man"[2] (see Fig. 9). The images were degraded by zero-mean Gaussian noise with STD $\sigma = 5, 10, 25, 40, 50, 80, 100$ dB. The images restored by two hybrid algorithms, denoted H1 and H2, were compared with BM3D-restored images based on PSNR and SSIM values[3] as well as visual perception. The diagrams in Fig. 10 illustrate the results of the experiments.

It is seen that although the PSNR values of all three algorithms are very close to each other, the SSIM achieved by the hybrid algorithms is significantly higher than that achieved by the BM3D. This is especially true for texture-rich images like "Fingerprint" and "Bridge". Figure 11 displays restoration of the "Bridge"

(a) "Fingerprint" (b) "Fabric" (c) "Bridge" (d) "Man"

Fig. 9 Original images

[2] These images were not reported in [5].

[3] We used the Matlab 2020b function `ssim.m` to calculate SSIM values.

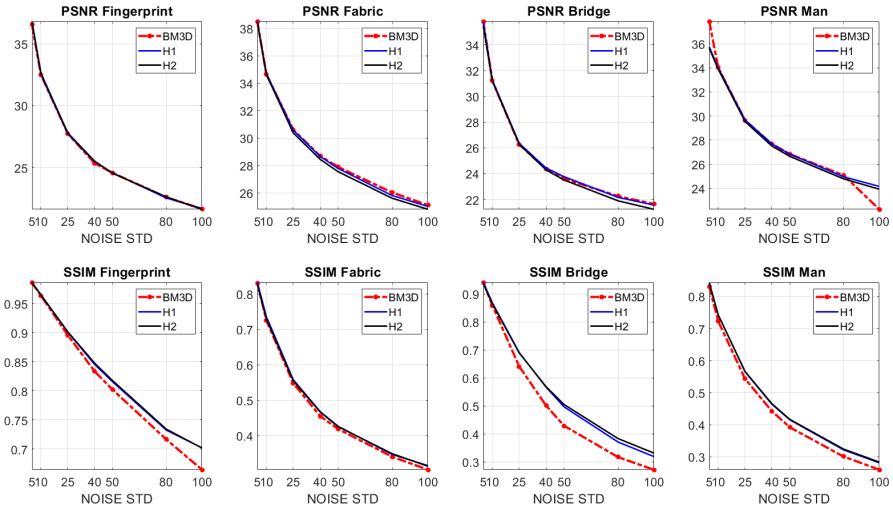

Fig. 10 Diagrams of PSNR and SSIM values for restoration of "Fingerprint", "Fabric", "Bridge" and "Man" images degraded by noise

image from the input degraded by Gaussian noise with STD $\sigma = 50$ dB. In this experiment, the image restored by H1 has PSNR = 23.76 dB and SSIM = 0.4963 vs. PSNR = 23.61 dB and SSIM = 0.4625 achieved by BM3D. Consequently, H1 managed to restore some fine structures which were blurred by BM3D. Figure 12 displays restoration of the "Fingerprint" image from the input degraded by strong Gaussian noise with STD $\sigma = 100$ dB. In this experiment, the image restored by H1 has PSNR = 21.68 dB and SSIM = 0.7019 vs. PSNR = 21.65 dB and SSIM = 0.6643 achieved by BM3D. Because of a strong noise, BM3D blurred some fragments of the image while H1 managed to restore them.

3.2 Image Inpainting

The designed qWPs demonstrated high efficiency in dealing with the image inpainting problem, that means restoration of images degraded by loss of significant share of pixels and possible addition of noise. State-of-the-art results in image inpainting were achieved by the iterative algorithm using decreasing thresholding values presented in [26, 25]. In [10], the performance of that algorithm with different filter banks was investigated. To be specific, the set *DAS-2*, *DAS-1* [28], *TP*-$\mathbb{C}TF_6$ and *TP*-$\mathbb{C}TF_6^{\downarrow}$ of filter banks, which we call SET-4 filter banks, were utilized. Note that for different types of images, different filter banks from the SET-4 were advantageous.

We designed a qWP-based iterative algorithm, which combines the split Bregman iteration scheme [14] with the adaptive decreasing thresholding. In multiple experiments on restoration of images corrupted by missing a large amount of pixels and

(a) Degraded image (b) Image restored by BM3D, PSNR = 23.61 dB and SSIM = 0.4625 (c) Image restored by H1, PSNR = 23.76 dB and SSIM = 0.4963

(d) Fragment of the image a (e) Fragment of the image b (f) Fragment of the image c

Fig. 11 Restoration of "Bridge" image from input degraded by Gaussian noise with STD $\sigma = 50$ dB

addition of Gaussian noise with various intensities, we compared the performance of our qWP-based algorithm with the performance of the SET-4 algorithms. The description of the algorithm and results of multiple experiments on image inpainting are presented in the paper [6]. The results are compared according to PSNR and SSIM values and by visual perception. Similarly to denoising experiments, the qWP algorithm prevailed in restoration of edges and fine structure even in severely degraded images. This fact is reflected in highest values of SSIM. A typical example is displayed in Fig. 13. In this example, the qWP restoration of the "Bridge" image[4] degraded by missing 50% of pixels and additive Gaussian noise with $\sigma = 50$ dB is compared with the restoration by DAS-2, which was the best out of the SET-4 algorithms.

4 Discussion

The paper describes the design of one- and two-dimensional quasi-analytic WPs (qWPs) originating from polynomial splines of arbitrary order and corresponding

[4] The "Bridge" image did not participate in the experiments presented in [6].

(a) Degraded image (b) Image restored by BM3D, PSNR = 21.65 dB and SSIM = 0.6643 (c) Image restored by H1, PSNR = 21.68 dB and SSIM = 0.7019

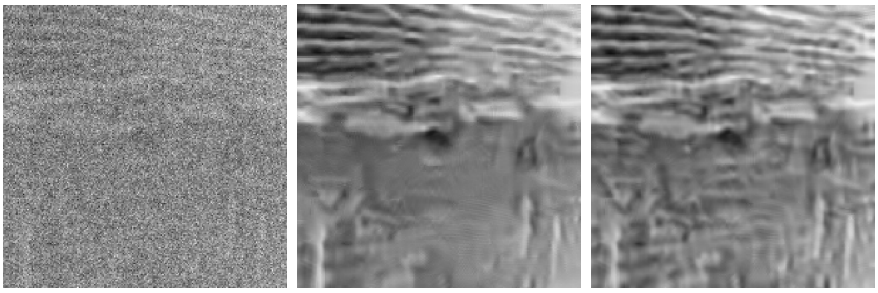

(d) Fragment of the image a (e) Fragment of the image b (f) Fragment of the image c

Fig. 12 Restoration of "Fingerprint" image from input degraded by Gaussian noise with STD $\sigma = 100$ dB

transforms. The qWP transforms operate in spaces of periodic signals. The periodic setting provides a lot of substantial opportunities for the design and implementation of WP transforms. The exceptional properties of the designed qWPs, such as waveforms' orientation in multiple directions combined with oscillations with multiple frequencies (to name a few) proved to be highly beneficial for the image restoration. Our experiments on image denoising and inpainting using qWP-based algorithms produced state-of-the-art results.

In summary, with this versatile and flexible tool, we are able to solve multiple data processing problems, such as image deblurring, superresolution, segmentation and classification, and target detection. In the latter, directionality is extremely important. Directional 3D wavelet packets under design can be useful in seismic and hyperspectral processing.

Acknowledgements This research was supported by the Israel Science Foundation (ISF, 1556/17), Len Blavatnik and the Blavatnik Family Foundation, Israel Ministry of Science Technology and Space (3-16414, 3-14481) and Academy of Finland (grant 311514).

(a) Clean image

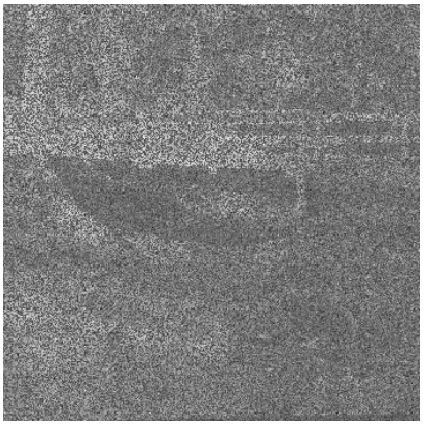

(b) Image degraded by missing 50% of pixels and Gaussian noise with $\sigma = 50\,\mathrm{dB}$

(c) Restoration by qWP, PSNR = 22.08 dB, SSIM = 0.3917

(d) Restoration by DAS-2, PSNR = 22.07 dB, SSIM = 0.3238

Fig. 13 Restoration of "Bridge" image

References

1. A. Averbuch, R. R. Coifman, D. L. Donoho, M. Israeli, and Y. Shkolnisky. A framework for discrete integral transformations I: The pseudopolar Fourier transform. *SIAM J. Sci. Comput.*, 30(2):764–784, 2008.
2. A. Averbuch, R. R. Coifman, D. L. Donoho, M. Israeli, Y. Shkolnisky, and I. Sedelnikov. A framework for discrete integral transformations II: The 2D discrete Radon transform. *SIAM J. Sci. Comput.*, 30(2):785–803, 2008.
3. A. Averbuch, P. Neittaanmäki, and V. Zheludev. *Splines and spline wavelet methods with applications to signal and image processing. Vol. III. Selected topics*. Springer, Cham, 2019.
4. A. Averbuch, P. Neittaanmäki, and V. Zheludev. Directional wavelet packets originating from polynomial splines. arXiv:2008.05364, 2020.

5. A. Averbuch, P. Neittaanmäki, V. Zheludev, M. Salhov, and J. Hauser. Coupling BM3D with directional wavelet packets for image denoising. arXiv: 2008.11595, 2020.
6. A. Averbuch, P. Neittaanmäki, V. Zheludev, M. Salhov, and J. Hauser. Image inpainting using directional wavelet packets originating from polynomial splines. *Signal Process. Image Commun.*, 97:116334, 2021.
7. I. Bayram and I. W. Selesnick. On the dual-tree complex wavelet packet and M-band transforms. *IEEE Trans. Signal Process.*, 56(6):2298–2310, 2008.
8. E. Candès, L. Demanet, D. Donoho, and L. X. Ying. Fast discrete curvelet transforms. *Multiscale Model. Simul.*, 5(3):861–899, 2006.
9. E. J. Candès and D. L. Donoho. New tight frames of curvelets and optimal representations of objects with piecewise C^2 singularities. *Commun. Pure Appl. Math.*, 57(2):219–266, 2004.
10. Z. Che and X. Zhuang. Digital affine shear filter banks with 2-layer structure and their applications in image processing. *IEEE Trans. Image Process.*, 27(8):3931–3941, 2018.
11. R. R. Coifman and M. V. Wickerhauser. Entropy-based algorithms for best basis selection. *IEEE Trans. Inform. Theory*, 38(2):713–718, 1992.
12. K. Dabov, A. Foi, V. Katkovnik, and K. Egiazarian. Image denoising by sparse 3-D transform-domain collaborative filtering. *IEEE Trans. Image Process.*, 16(8):2080–2095, 2007.
13. M. N. Do and M. Vetterli. Contourlets. In G. V. Welland, editor, *Beyond Wavelets*, pages 83–105. Academic Press, San Diego, CA, 2003.
14. T. Goldstein and S. Osher. The split Bregman method for $L1$-regularized problems. *SIAM J. Imaging Sci.*, 2(2):323–343, 2009.
15. B. Han, Q. Mo, Z. Zhao, and X. Zhuang. Directional compactly supported tensor product complex tight framelets with applications to image denoising and inpainting. *SIAM J. Imaging Sci.*, 12(4):1739–1771, 2019.
16. B. Han and Z. Zhao. Tensor product complex tight framelets with increasing directionality. *SIAM J. Imaging Sci.*, 7(2):997–1034, 2014.
17. B. Han, Z. Zhao, and X. Zhuang. Directional tensor product complex tight framelets with low redundancy. *Appl. Comput. Harmon. Anal.*, 41(2):603–637, 2016.
18. A. Jalobeanu, L. Blanc-Féraud, and J. Zerubia. Satellite image deconvolution using complex wavelet packets. In *Proceedings 2000 International Conference on Image Processing*, pages 809–812. IEEE, 2000.
19. H. Ji, Z. Shen, and Y. Zhao. Directional frames for image recovery: Multi-scale discrete Gabor frames. *J. Fourier Anal. Appl.*, 23(4):729–757, 2017.
20. H. Ji, Z. Shen, and Y. Zhao. Digital Gabor filters with MRA structure. *Multiscale Model. Simul.*, 16(1):452–476, 2018.
21. N. Kingsbury. Image processing with complex wavelets. *Phil. Trans. R. Soc. A*, 357(1760):2543–2560, 1999.
22. G. Kutyniok and D. Labate, editors. *Shearlets: Multiscale analysis for multivariate data*. Birkhäuser Boston, 2012.
23. G. Kutyniok, W.-Q. Lim, and X. Zhuang. Digital shearlet transforms. In *Shearlets: Multiscale analysis for multivariate data*, pages 239–282. Birkhäuser Boston, 2012.
24. I. W. Selesnick, R. G. Baraniuk, and N. C. Kingsbury. The dual-tree complex wavelet transform. *IEEE Signal Process. Mag.*, 22(6):123–151, 2005.
25. Y. Shen, B. Han, and E. Braverman. Image inpainting using directional tesnor product complex tight framelets. arXiv: 1407.3234, 2014.
26. Y. Shen, B. Han, and E. Braverman. Image inpainting from partial noisy data by directional complex tight framelets. *ANZIAM J.*, 58(3–4):247–255, 2017.
27. Z. Wang, A. C. Bovik, H. R. Sheikh, and E. P. Simoncelli. Image quality assessment: From error visibility to structural similarity. *IEEE Trans. Image Process.*, 13(4):600–612, 2004.
28. X. Zhuang. Digital affine shear transforms: Fast realization and applications in image/video processing. *SIAM J. Imaging Sci.*, 9(3):1437–1466, 2016.